Journal of Nuclear Materials 403 (2010) 135–146

Contents lists available at ScienceDirect

Journal of Nuclear Materials

journal homepage: www.elsevier.com/locate/jnucmat

Experimental study and numerical modelling of the irradiation damage recovery in zirconium alloys

J. Ribis [a,*], F. Onimus [a], J.-L. Béchade [a], S. Doriot [a], A. Barbu [b], C. Cappelaere [c], C. Lemaignan [d]

[a] CEA-DEN/SRMA, CEA/Saclay, 91191 Gif-sur-Yvette, France
[b] CEA-DEN/SRMP, CEA/Saclay, 91191 Gif-sur-Yvette, France
[c] CEA-DEN/SEMI, CEA/Saclay, 91191 Gif-sur-Yvette, France
[d] CEA-DEC, CEA/Grenoble, 38054 Grenoble Cedex, France

ARTICLE INFO

Article history:
Received 21 October 2009
Accepted 7 June 2010

ABSTRACT

Neutron irradiation damage in zirconium alloys used as fuel cladding tubes for Pressurized Water Reactors in the nuclear industry consists mainly in a high density of small prismatic dislocation loops. During post-irradiation heat treatment thermal annealing of loops occurs. This phenomenon has been investigated by transmission electron microscopy and microhardness tests. It has been shown that the loop density decreases while their mean size increases. Furthermore it was demonstrated that only vacancy loops remain present in the material after a long term annealing at high temperature. A mechanism based on vacancies diffusion has been proposed to explain the loop evolution during annealing. A cluster dynamic model, originally developed to compute the evolution of the microstructure under irradiation, has been adapted to the modelling of the annealing for zirconium alloys. This physically based model reproduces the loop size and density evolution during a large variety of heat treatments and also provides a better understanding of the mechanisms involved in the loop recovery.

1. Introduction

Zirconium alloys are commonly used in Pressurized Water Reactors (PWR) as fuel rod cladding tubes. After in-reactor use, the spent nuclear fuel is stored in water and can eventually be transported to a long term storage pool facility. During transportation in dry cask, the cladding is the last confinement barrier before radionuclide release. The main risk of rupture at high temperature is due to cladding creep under the internal pressure of fission gases and the temperature due to residual power of the fuel [1]. During post-irradiation creep, the cladding is subjected to heat treatments combined with an applied stress [2] that can affect the irradiation induced microstructure as well as the mechanical properties.

In order to have a better understanding of both the effect of a heat treatment on the mechanical properties and the post-irradiation creep deformation mechanisms, a thorough study of the irradiation defects recovery in recrystallized zirconium alloys has been performed. However, because of complex coupling that can arise between thermal recovery and deformation, the understanding of the post-irradiation creep behaviour requires also the study of the creep deformation mechanisms as it has been done elsewhere [2].

At the microscopic scale, it is known that neutron irradiation damage in zirconium alloys consist mainly in a high density of small prismatic dislocation loops. These loops have a Burgers vector $\langle a \rangle$ and their habit plane is close to the first order prism plane $\{1\,0\,\bar{1}\,0\}$ [3–5]. It is also noteworthy that contrary to most of irradiated metals, both interstitial and vacancy loops can coexist in zirconium alloys [3–5].

At the macroscopic scale, this high density of loops results in an increase in the yield strength and a decrease of ductility of the material [6–8] because of the strong interaction between gliding dislocations and loops [9–11].

It has been shown by various authors that a post-irradiation heat treatment performed at a temperature above the irradiation temperature can lead to the recovery of the radiation induced hardening [12–17]. Also heat treatments lead to the annealing of the radiation induced loops [17,18]. However, this phenomenon has usually not been studied for similar duration and temperature as for the creep tests. In addition clear understanding and modelling of the recovery mechanisms of the irradiation damage are still lacking.

For a better understanding and prediction of the irradiation defects recovery, post-irradiation heat treatments have been performed on a recrystallized zirconium alloy. After the heat treatments, the evolutions of the loop diameters and densities have been characterized using transmission electron microscopy (TEM). In addition, microhardness tests performed at room temperature have been used to measure the recovery of the irradiation hardening. This recovery is then correlated to TEM observations. Thanks

* Corresponding author. Tel.: +33 1 69 08 85 09; fax: +33 1 69 08 71 30.
E-mail address: joel.ribis@cea.fr (J. Ribis).

0022-3115/$ - see front matter © 2010 Elsevier B.V. All rights reserved.
doi:10.1016/j.jnucmat.2010.06.012

to a thorough TEM characterization of the evolution of the proportion of vacancy and interstitial loops during the heat treatment, the recovery mechanism is discussed. Finally, a physically based cluster dynamic model is used to reproduce the microstructure and the microhardness evolutions. The computations are compared to both experimental data and theory.

2. Materials and experimental details

The studied material is a recrystallized annealed zirconium alloy, with main alloying elements: 1200 ppm oxygen, 237 ppm iron and 1% niobium. Due to the fabrication process and the plastic anisotropy of the hexagonal closed packed structure of α-zirconium, cladding tubes made of zirconium alloys are strongly textured from crystallographic point of view. The $\langle c \rangle$ axis is close to the radial direction [19] and inclined up to 30° in the $(r–\theta)$ plane. The materials studied have been irradiated between 320 °C and 350 °C in PWR up to fluences (>1 MeV) of 11×10^{25} n m^{-2} (5 PWR cycles). The Vickers microhardness experiments have been carried out using a 200 g load on the cross sections along the $(r–\theta)$ plane of the tube. In order to provide statistical results, 10 hardness measurements have been performed for each sample at room temperature. TEM observations were performed on a Philips EM 430 microscope operating at 300 kV. The annealing conditions for samples studied by microhardness tests and TEM observations are given in Table 1.

3. Experimental results and discussion on the recovery mechanism

3.1. Hardness evolution during annealing

Microhardness results are given in Table 2 and Fig. 1. In Table 2 it can be noticed that the irradiation hardness increment is equal to: $\Delta H_v = 76$ kg mm^{-2}. This value is close to the values obtained by Nakatsuka and Nagai [20] and Adamson and Bell [17]. These authors have measured an irradiation hardness increment value around 80 kg mm^{-2} for recrystallized annealed Zircaloy-2 samples irradiated up to a fluence of 2.8×10^{25} n m^{-2} (1 PWR cycle) for Nakatsuka and Nagai [20] and up to a fluence of 6.5×10^{24} n m^{-2} (<1 PWR cycle) for Adamson and Bell [17].

Table 1
Annealing conditions for microhardness tests and TEM observations of the studied alloy.

Annealing time (h)	Annealing temperature (°C)		
50	350	400	–
100	350	400	–
250	350*	400*	–
500	350*	400*	–
960	–	–	450*

* TEM observations.

Table 2
Microhardness results.

Annealing time (h)	Hardness (kg mm^{-2})		
	350 °C	400 °C	450 °C
Non-irradiated	161	161	161
As-irradiated	237	237	237
50	229	209	–
100	224	205	–
250	209	190	–
500	199	184	–
960	–	–	182

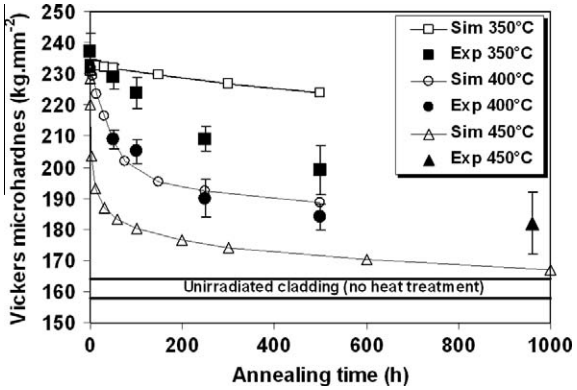

Fig. 1. Evolution of the experimental (Exp) microhardness after heat treatments and comparison with the modelling (Sim).

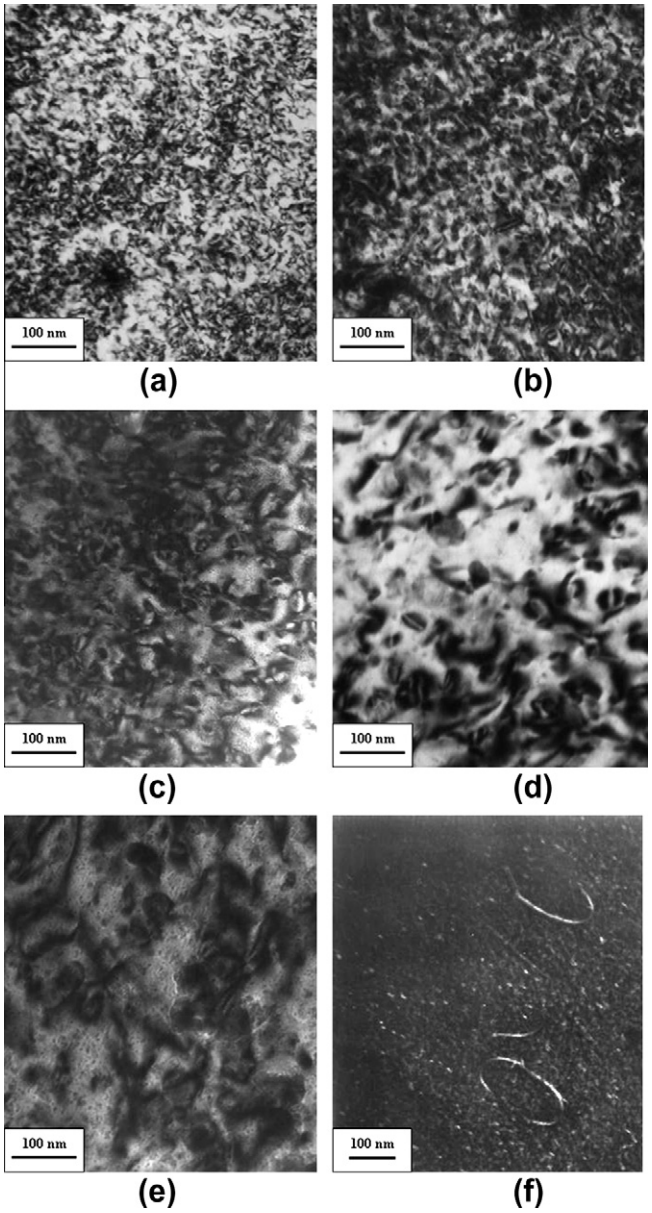

Fig. 2. Microstructure of the material (a) as-irradiated, after annealing of (b) 250 h at 350 °C, (c) 500 h at 350 °C, (d) 250 h at 400 °C, (e) 500 h at 400 °C, (f) 960 h at 450 °C. The pictures are shown in bright field diffraction condition except (f) which is obtained in weak beam conditions.

It can be seen on Fig. 1 that the hardness of the material progressively decreases with time during the annealing. The kinetics of this softening is fast in the first hours and then tends to slow down progressively until nearly reaching the non-irradiated microhardness value. However, after 960 h at 450 °C the hardness of the material is still not fully recovered, i.e. the hardness has not reached the non-irradiated hardness value.

It is also seen in Fig. 1 that the kinetics of the recovery is increased by the temperature showing that the recovery mechanism of the irradiation damage is thermally activated.

3.2. Microstructure evolution during annealing

TEM observations have been performed for the as-irradiated material and for five heat treated samples (Table 1). The loop microstructure (diameters ($\langle d \rangle$) and densities (N)) has been studied quantitatively by TEM. Typical TEM pictures of each sample are reported in Fig. 2. It is shown on the Table 3 and Fig. 3 that the loop densities (N) decrease during the annealing while the mean loop diameters ($\langle d \rangle$) increase. The thin foil thickness has been estimated to a value of 150 nm ± 50 nm using stereographic measurement. This estimation induces an error on the value of the loop density measured in addition to the uncertainty of the number of loops measured. Concerning the diameter of the loops the error is induced by the accuracy of the measurement on the micrograph. The errors are given in Table 3. It has also to be pointed out that the very small objects, with diameter less than 2 nm, can hardly be observed by TEM and none are reported here. The mean loop diameter measured in the as-irradiated material is slightly larger than the mean loop diameter measured by Northwood et al. [3], but this difference can be explained by the difficult observation of $\langle a \rangle$ loops in this material due to the high loop density.

On the Fig. 4 the cumulated distributions of loops measured for each sample are reported. The cumulated distributions obtained after annealing show both a shift of the distribution toward larger loops and also a broadening of the distributions. The extreme situation is obtained for the sample annealed at 450 °C for 960 h where the loops have very large diameter, higher than 100 nm, and a very low density (few loops are observed in each grain).

In order to understand the mechanism for loop annealing, it is necessary to know how the different types of loops (vacancy and interstitial) evolve during the heat treatments. The evolution of these two types of loops has been studied by TEM using the inside/outside contrast method [18,21,22]. The zone axis used for this study is $B = \langle 1\,1\,\bar{2}\,3 \rangle$ and the diffraction vector used is $\vec{g} = 1\,\bar{2}\,1\,\bar{2}$. Due to the orientation of this diffraction vector, the orientation of the loops relative to this vector is only needed to determinate the nature of the loop. Depending on the habit plane of loops, the Burgers vector $\vec{b}$, the diffraction vector $\vec{g}$, and the nature of the loop, the loops studied exhibit different contrasts, either an inside or an outside contrast. As it can be shown on Fig. 5a, vacancy loops (V on the picture) exhibit an inside contrast and on the Fig. 5b, these loops exhibit an outside contrast.

Due to a high density of loops in the as-irradiated material, the TEM observation conditions do not allow to perform the loop nature identification. However, from literature data it can be seen that roughly 50% of the loops present in the material are interstitial loops and 50% are vacancy loops for an irradiation temperature around 350 °C [23].

TEM observations have been performed on the samples heat treated. The loop nature has been characterized and the results

Table 3
Mean diameter and density of loops for various annealing conditions.

Annealing temperature (°C)	Annealing time (h)	$\langle d \rangle$ (nm)	N (m^{-3})
–	0	14.0 (±1.4)	$1.2\ (\pm 0.4) \times 10^{22}$
350	250	17.0 (±1.7)	$3.2\ (\pm 1.7) \times 10^{21}$
350	500	20 (±2)	$3.3\ (\pm 1.1) \times 10^{21}$
400	250	18.0 (±1.8)	$2.5\ (\pm 1.2) \times 10^{21}$
400	500	24.0 (±2.4)	$1\ (\pm 0.4) \times 10^{21}$
450	960	176 (±17)	$1.2\ (\pm 0.6) \times 10^{20}$

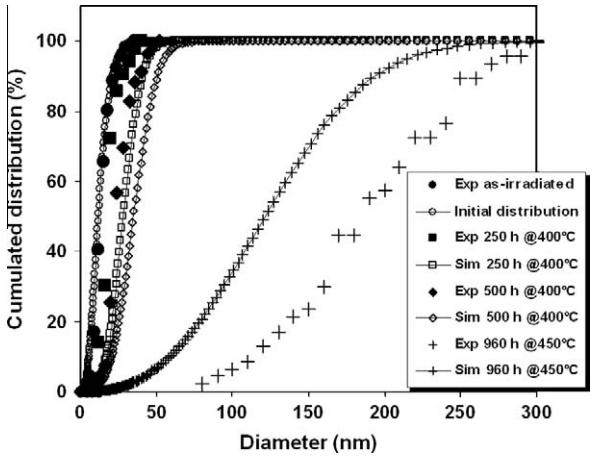

Fig. 4. Cumulated distributions for various annealing conditions. Experiment (Exp) and modelling (Sim).

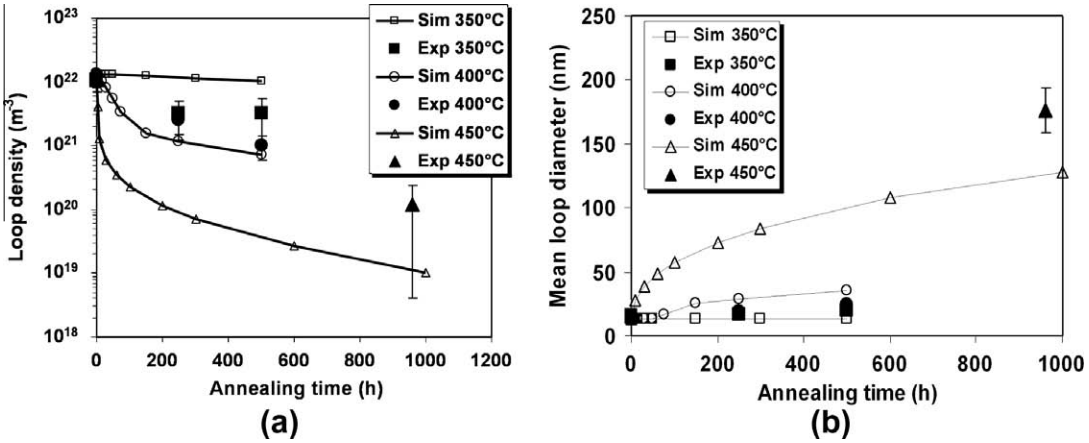

Fig. 3. Evolution of: (a) the loop density and (b) the loop diameter during a thermal annealing at 350 °C, 400 °C and 450 °C. Experiment (Exp) and modelling (Sim).

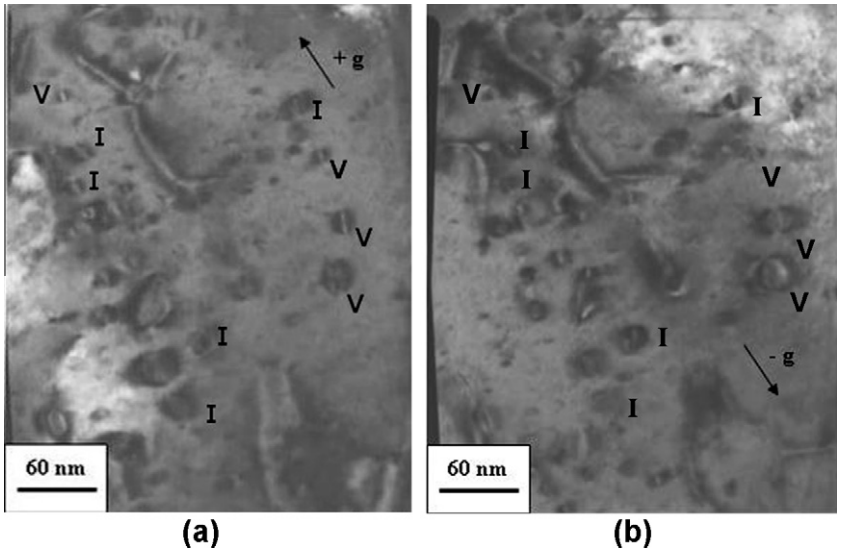

Fig. 5. Microstructure after annealing at 400 °C during 240 h, change of loop contrast when imaging with diffraction vector: (a) $+\vec{g} = 1\bar{2}1\bar{2}$ and (b) $-\vec{g} = \bar{1}2\bar{1}2$.

are presented on Table 4. The tendency is that the interstitial loops are rapidly annealed during the heat treatment whereas vacancy loop annealing occurs slowly, leading progressively to a microstructure only composed of large vacancy loops in very low densities. These results are in good agreement with the results presented by Kelly and Blake [18] who have shown that the interstitial loops disappear during annealing.

3.3. Correlation between the microhardness and the loop microstructure

It is known that the irradiation induced loops lead to a strong hardening of metals. A simple hardening model [24,25] shows that the critical resolved shear stress (τ_c) of the material increases after irradiation by an increment $\Delta\tau_c$, which can be expressed as:

$$\Delta\tau_c = \alpha\mu b\sqrt{N\langle d\rangle} \tag{1}$$

where α is a coefficient characteristic of the strength of the obstacle, μ is the shear modulus, b is the Burgers vector, N is the density of loops and $\langle d\rangle$ is the mean loop diameter. The critical shear stress can be related to the yield stress by considering that the Taylor factor theory can also be applied to zirconium alloys, in a first approximation ($\sigma_y = M\tau_c$, where σ_y is the yield stress, τ_c the critical shear stress and M the Taylor factor). Furthermore, it is known that there is a linear relationship between the yield stress and the Vickers hardness [26] ($\Delta H_v = C\Delta\sigma_y$, where ΔH_v is the hardness increment, $\Delta\sigma_y$ the yield stress increment and C a proportionality coefficient).

Table 4
Evolution of the proportion of vacancy loops during annealing. Experimental results and modelling.

Annealing temperature (°C)	Annealing time (h)	Experiment		Modelling
		Number of analysed loops	Percentage of vacancy loops (%)	Percentage of vacancy loops (%)
As-irradiated	As-irradiated	–	50 [23]	50
350	250	19	50	45
350	500	24	50	43
400	250	37	65	100
400	500	38	71	100
450	960	13	100	100

The hardness increment can thus be expressed as the following expression [25]:

$$\Delta H_v = CM\alpha\mu b\sqrt{N\langle d\rangle} \tag{2}$$

According to Busby et al. [26] the proportionality coefficient C, between the yield stress and the hardness, is close to 0.3.

From the experimental data obtained during the heat treatments it is possible to check whether this simple model is valid in the case of neutron irradiated zirconium alloys. This can also provide a valuable tool to predict the softening of the material during a heat treatment from the knowledge of its loop microstructure.

The measured hardness increment ΔH_v is plotted on Fig. 6 as a function of $\sqrt{N\langle d\rangle}$, where the N and $\langle d\rangle$ values are obtained from TEM observations. It is seen on Fig. 6 that, taking into account the uncertainty of the loop density measurement, the linear relationship is acceptable, therefore confirming the validity of this simple hardening model. Furthermore the numerical value of $CM\alpha\mu b$ obtained from the linear regression is equal to 5.4×10^{-9} kg mm^{-1}. This value is in good agreement with the value computed from the experimental results obtained by Adamson and Bell [17] on recrystallized annealed Zy-2, which is 5×10^{-9} kg mm^{-1}. From this value, it is possible to compute the coefficient characteristic of the obstacle strength (α) of the loops. The shear modulus (μ) at room temperature is equal to 3.6×10^4 MPa according to [27]. The Burgers vector of the $\langle a\rangle$ dislocation loop is $b = 3.232$ Å. Therefore, the value of the product of the coefficients $M\alpha$ is equal to 1.55. Considering that the Taylor factor (M) for textured zirconium alloys lies between 2 [28] and 4 [29], a value for the strength of the obstacles (α) is then obtained between 0.39 and 0.78, which is in good agreement with the literature data [25].

From this simple model it can be seen that the progressive softening during the heat treatment is directly related to the decrease of the loop density during the recovery. However, the increase of the mean diameter also plays a role in the resulting hardening. As it will be shown in the following sections, this model can be used to predict the hardness of the material from the knowledge of its loops microstructure.

However, the irradiation induced hardening of the material is still not fully recovered after 960 h at 450 °C (Fig. 1). Indeed, the hardness of the material is still higher than the hardness of the non-irradiated material. This residual hardening could be

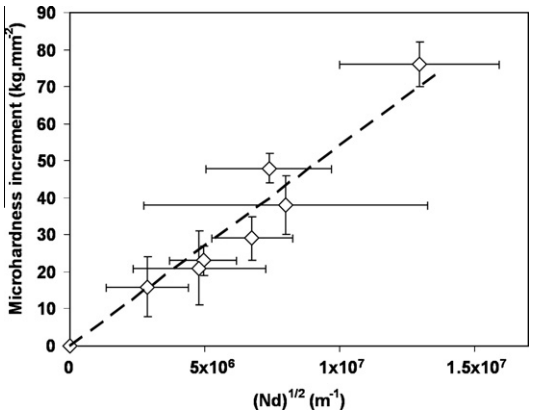

Fig. 6. Microhardness increment evolution as a function of $(N\langle d\rangle)^{1/2}$.

explained by the irradiation-enhanced precipitation of β-Nb in the material [30]. Indeed, it is seen that the small needle-like precipitates formed during irradiation are still present in the material after the heat treatment. They appear as white dots in Fig. 2f. Since the density of the precipitates is high this can create a residual hardening as shown by numerical computation [31]. The equation (Eq. (2)) can also be applied to the hardening induced by the precipitates. Experimental measures of the density of precipitates $N_p = 1.7 \times 10^{22}$ m^{-3} and mean diameter of precipitates $d_p = 3.6$ nm [30] can be used to estimate the obstacle strength of the precipitates from the experimental residual hardness. With the same values used previously it can be seen that the obstacle strength (α) of the precipitate lies in between 0.02 and 0.04. This value seems to be much lower than values obtained by theoretical approach [31].

3.4. Discussion on the recovery mechanism

The TEM observations have shown that during the heat treatments the vacancy loops grow and the density of vacancy loops decreases and in the same time the interstitial loops progressively disappear. Besides, for a long term annealing performed at 450 °C, only large vacancy loops with very low density remain in the material. A mechanism involving bulk diffusion of vacancies has been proposed by various authors [32–37] in order to explain the loop growth or shrinkage during the post-irradiation annealing of metals. However, those authors have usually not taken into account the possibility that both types of loops, vacancy and interstitial, can be present in the material at the same time. In the following, a recovery mechanism occurring when both interstitial and vacancy loops are present simultaneously is proposed.

When the bulk diffusion mechanism is operative, loop growth or shrinkage occurs by diffusion of point defects to and from the loops via the matrix. Due to the high mobility of self-interstitial atoms (SIA) they disappear rapidly when the irradiation stops. In addition, due to their high formation energy the SIA cannot be emitted from loops. Consequently the recovery of loops is only controlled by the vacancy diffusion. The emission or absorption of a vacancy by a perfect loop results in a change in its elastic energy. According to Hirth and Lothe [36], the elastic energy of a circular loop with the Burgers vector normal to the plane of the loop is given by:

$$W = 2\pi r \frac{\mu b^2}{4\pi(1-\nu)}\left(\ln\left(\frac{4r}{r_{core}}\right) - 1\right) \tag{3}$$

where r the radius of the loop, μ the shear modulus, ν the Poisson's ratio, b the modulus of the Burgers vector and r_{core} the core radius which can be taken as $r_{core} = b$ [36]. The number of vacancy n in a vacancy loop with radius r is $n = \pi\, r^2 b/V_{at}$. Therefore if a vacancy loop contracts by an amount δr, the number of emitted vacancies is $\delta n = 2\pi b r \delta r/V_{at}$.

The elastic energy release per emitted vacancy is then:

$$w = \frac{\partial W}{\partial n} = \frac{\partial W}{\partial r}\frac{\partial r}{\partial n} = 2\pi\tau\frac{\partial r}{\partial n} = \frac{\tau V_{at}}{rb} \tag{4}$$

where τ is the line tension of the dislocation loop given by Hirth and Lothe [36] as:

$$\tau = \frac{\partial W}{2\pi\partial r} = \frac{\mu b^2}{4\pi(1-\nu)}\ln\left(\frac{4r}{r_{core}}\right) \tag{5}$$

For the loop to be in local equilibrium with the vacancies, w must equal the local value of the chemical potential for vacancies:

$$w = kT\ln\left(\frac{c_v}{c_v^0}\right) \tag{6}$$

where c_v^0 is the thermal equilibrium concentration of vacancies in the bulk crystal, k is Boltzmann's constant and T the annealing temperature.

As it has been pointed out by Eyre and Maher [35], the concentration of vacancies in local equilibrium with the vacancy loop is therefore:

$$c_v^{vl} = c_v^0 \exp\left(\frac{\tau V_{at}}{rbkT}\right) \tag{7}$$

This shows that the vacancy concentration around a vacancy loop is higher than the thermal equilibrium vacancy concentration ($c_v^{vl} > c_v^0$). This means that an isolated vacancy loop in the matrix shrinks due to the emission of vacancies. However, in the case of a super-saturation of vacancies, the vacancy loop can grow, depending on its radius and on the super-saturation. The growth rate of the vacancy loop can be expressed as Eq. (8), by solving the diffusion problem [35]:

$$\frac{dr}{dt} = AD_S\left[\frac{c_v}{c_v^0} - \exp\left(\frac{\tau V_{at}}{rbkT}\right)\right] \tag{8}$$

where A is a geometrical coefficient and D_S is the self-diffusion coefficient.

For a given super-saturation (c_v/c_v^0), a vacancy loop with a radius r higher than a critical radius r_{crit} will grow and vice versa. Then following the approach of Eyre and maher [35], the critical radius r_{crit} is given by Eq. (9):

$$r_{crit} = \frac{\tau V_{at}}{bkT\ln\left(\frac{c_v}{c_v^0}\right)} \tag{9}$$

In the case of interstitial loops, vacancy emission results in an increase of the loop radius and therefore in an increase of the elastic energy of the loop and the concentration of vacancies in local equilibrium with the interstitial loops is then:

$$c_v^{il} = c_v^0 \exp\left(-\frac{\tau V_{at}}{rbkT}\right) \tag{10}$$

This shows that the vacancy concentration around an interstitial loop is lower than the thermal equilibrium vacancy concentration ($c_v^{il} < c_v^0$) and the interstitial loops always shrink whatever their radii.

In the material, the loops are not isolated but they are embedded into a medium containing many vacancy sources and sinks. Therefore all the vacancy sources and sinks have to be taken into account in order to describe the recovery mechanism. Due to the vacancy gradients between the various types of loops with various sizes, several vacancy fluxes are taking place in the material. In addition, it can be seen that the vacancy concentration at the

vicinity of the grain boundaries is equal to the thermal equilibrium vacancy concentration c_v^0. Therefore vacancy fluxes also occur between the loops and the grain boundaries. All these vacancy flux are listed below:

- A vacancy flux from the vacancy loops to the grain boundaries ($c_v^{vl} > c_v^0$), that act as sink for vacancies, leading to the progressive disappearance of vacancy loops.
- A vacancy flux from the vacancy loops to the interstitial loops ($c_v^{il} < c_v^{vl}$) which leads also to the disappearance of the vacancy loops and also the shrinkage of the interstitial loops.
- A vacancy flux from the grain boundaries (c_v^0), which act as sources for vacancies, to the interstitial loops ($c_v^{il} < c_v^0$), also leading to the shrinkage of interstitial loops.

In addition, since the vacancy concentration around a vacancy loop is expressed as $c_v^{vl} = c_v^0 \exp(\tau V_{at}/rbkT)$, the vacancy concentration around small vacancy loops is higher than around large vacancy loops ($c_v^{vl}(r_1) > c_v^{vl}(r_2)$ for $r_1 < r_2$). Due to this difference in the local vacancy concentration around vacancy loops of various sizes, another vacancy flux takes place from small vacancy loops to large vacancy loops. Consequently, the biggest vacancy loops grow at the expense of the smallest ones. For this reason, at the same time that interstitial and small vacancy loops shrink ($r < r_{crit}$), the biggest vacancy loops grow ($r > r_{crit}$). This mechanism therefore explains that at the end of the heat treatment performed at 450 °C, only large vacancy loops in low density are observed and no more interstitial loops are present in the material.

4. Numerical modelling of the recovery of loops

4.1. Cluster dynamic modelling

The prediction of the recovery of the loop microstructure requires taking into account all the vacancy sources and sinks in the material in order to compute the vacancy concentration during the heat treatments. The numerical model chosen to simulate and predict the evolution of the microstructure during a heat treatment is based on the homogeneous rate theory applied to clusters dynamics. Such modelling has been developed by Duparc et al. [38] and applied to zirconium by Christien et al. [39] by taking into account the anisotropic diffusion of self-interstitial atoms (SIA). More recently Christien et al. [40] have applied the cluster dynamic model in order to compute the growth of zirconium single crystal. Dubinko et al. [41] have also developed a cluster dynamic modelling, based on isotropic diffusion of point defects, to the microstructure evolution in zirconium alloys but they adopted a different approach for the calculation of the loop and dislocation biases in order to simulate the coexistence of both interstitial and vacancy loops.

Clusters dynamics is based on kinetic equations describing the formation and evolution of clusters of point defects such as vacancies or SIA. The efficiency of this modelling comes from the basic hypothesis of uniform spatial distributions of clusters. Indeed, the real system is replaced by an effective medium in which all processes occur continuously in time and space. The spatial correlations between clusters are consequently not explicitly considered. The system is seen as a gas of clusters that can be either vacancies or interstitials within a single crystal grain of the polycrystalline metal. However, the mechanical interactions between the grains are neglected in this model. The evolution of the density of clusters of each size n and of a certain kind is modelled within the framework of the chemical rate theory and it is described by a set of differential equations of the form:

$$\frac{dC_n}{dt} = G_n + \sum_m J_{m\to n} - \sum_q J_{n\to q} - K_n C_n \tag{11}$$

where G_n is the production rate of defect of class n, K_nC_n is the eliminating rate on sinks, C_n is the cluster density of size n and $J_{m\to n}$ the cluster flux from the class of size m to the class n. The flux $J_{m\to n}$ is given by:

$$J_{m\to n} = \sum_m w_{m\to n} C_m \tag{12}$$

With $w_{m\to n}$ the transition rate from the class of size m to the class of size n. Assuming that only point defects (SIA and vacancies) are mobile, Eq. (11) may be rewritten as follows:

$$\left.\begin{aligned} \frac{dC_{ni}}{dt} &= G_{ni} + \left[\beta^i_{(n-1)i}C_{1i} + \alpha^v_{(n-1)i}\right]C_{(n-1)i} + \left[\beta^v_{(n+1)i}C_{1v} + \alpha^i_{(n+1)i}\right]C_{(n+1)i} - \left[\alpha^i_{ni} + \beta^v_{ni}C_{1v} + \alpha^v_{ni} + \beta^i_{ni}C_{1i}\right]C_{ni} \\ \frac{dC_{nv}}{dt} &= G_{nv} + \left[\beta^v_{(n-1)v}C_{1v}\right]C_{(n-1)v} + \left[\beta^i_{(n+1)v}C_{1i} + \alpha^v_{(n+1)v}\right]C_{(n+1)v} - \left[\alpha^v_{nv} + \beta^v_{nv}C_{1v} + \beta^i_{nv}C_{1i}\right]C_{nv} \end{aligned}\right\}, \quad n > 2 \tag{13}$$

Here $C_{n\theta}$ is the concentration (number per unit volume) of clusters containing n point defects (size n) of type θ (θ and $\theta' = i$ for SIA and v for vacancy), $G_{n\theta}$ (with $n \leqslant 20$) is the production rate of small point defects clusters ($m^{-3}\ s^{-1}$) inside displacements cascade under irradiation, $\beta^{\theta'}_{n\theta}C_{1\theta'}$ is the rate of capture of a point defect of type θ' by a cluster of type θ and size n, $\alpha^{\theta'}_{n\theta}$ is the rate of emission of a point defect of type θ' by a cluster of type θ and size n .

Only the emission of vacancies by vacancy loops is taken into account, the emission of SIA by vacancy loops is neglected in the modelling due to the high formation energy of the SIA. The emission and capture rates include the physical parameters such as the diffusion coefficient ($D_\theta = D_{\theta 0}\exp(-E^m_\theta/kT)$) and the energy of point defect formation (E^f_θ). The detailed equations and coefficients of the model for isotropic diffusion are reported in the Appendix A.

In order to apply this model to zirconium, Christien et al. [39] have taken into account the anisotropic diffusion of SIA mainly by taking into account the effect of the orientation of the dislocation lines with respect to the $\langle a\rangle$ and $\langle c\rangle$ axis into the efficiency factor for absorption of point defects by loops. In this present work the anisotropic model [39] is used. However, because of the high formation energy of SIA, the contribution of SIA diffusion is believed to remain negligible, the model being therefore essentially isotropic.

It is indeed possible to use this model to compute the recovery of loops during a heat treatment by choosing the production rate of point defects and point defect clusters equals to zero ($G_n = 0, \quad n \geqslant 1$). However, the initial microstructure has to be in good agreement with the TEM observations of the as-irradiated microstructure. It turns out that it is rather difficult to obtain both vacancy and interstitial loops with the appropriate size and density using the same consistent coefficients than those used for the recovery. In order to simplify the fitting process, in this first approach, it was chosen to introduce an "ad hoc" initial microstructure that corresponds to the microstructure observed by TEM after irradiation. However, the accurate determination of the vacancy and interstitial loop mean diameter and density has not been performed for the as-irradiated microstructure. In addition, only the size distribution for loops with diameter higher than 2 nm

has been measured. Therefore assumptions have to be made concerning the respective vacancy and interstitial loop size distributions. The details concerning the introduction of the initial microstructure is given in Appendix B.

4.2. Fitting and comparison with experimental results

Starting from the initial microstructure, the heat treatments are simulated and only one coefficient of the model is adjusted in order to reproduce the experimental results obtained after annealing. In a first step, the coefficients adopted are the same as the coefficients given by Christien et al. [39]. Only the thin foil thickness is replaced by the experimental grain size of the recrystallized zirconium (d_g = 10 μm) using the appropriate formula for the absorption rate by grain boundaries (Appendix A). However this coefficients set is not able to reproduce properly the loop recovery. This can be explained by the fact the materials studied are different (good purity Van Arkel zirconium modelled by Christien et al., Zr–1%Nb–O alloy in this work). The difference can also be explained by the fact that the cluster dynamic model is based on the assumption that the mechanisms take place homogeneously in the material whereas defects creation in displacement cascade during irradiation is heterogeneous. On the contrary thermal recovery occurs homogeneously inside the crystal grains and is therefore better suited to be modelled by cluster dynamic model. In order to have a correct description of the loop recovery, the pre-exponential vacancy diffusion coefficient (D_{0v}) is adjusted on the experimental data obtained during a heat treatment performed at 400 °C. The coefficients used in the modelling are given in Table 5. The pre-exponential diffusion coefficient obtained with a good sensitivity is $D_{0v} = 2 \times 10^{-4}$ m^2 s^{-1}. This pre-exponential diffusion coefficient provides a value for the self-diffusion coefficient between the values given in [42] and the values obtained in [43,44] for pure α-zirconium. It has to be pointed out that complex effects of iron [45,46] and niobium [47,48] on the vacancy mobility has been neglected in this modelling.

The Fig. 3 represents the density and size evolution of loops during the thermal annealing, compared to the TEM observations. The evolution of the loop density obtained by the simulation is relatively close to the experimental values considering the uncertainties. The main discrepancy is obtained for the recovery performed at 350 °C where the predicted recovery is very low compared to the experiment. Concerning the diameter, the modelling is correct except for the heat treatment performed at 450 °C where the predicted size is slightly lower than the experiment.

Table 5
Main dynamic cluster model input coefficient.

	Symbol	Value	Ref.
Grain size	d_g	10^{-5} m	Experiment
Vacancy formation energy	E_f^v	1.79 eV	[39]
Vacancy migration energy	E_m^v	0.93 eV	[39]
Pre-exponential vacancy diffusion coefficient	D_{0v}	2×10^{-4} m^{2}s^{-1}	Adjusted
Interstitial formation energy	E_f^i	3.77 eV	[39]
Interstitial migration energy along the *c*-axis	$E^i_{m\langle c\rangle}$	0.15 eV	[39]
Interstitial migration energy along the *a*-axis	$E^i_{m\langle a\rangle}$	0.06 eV	[39]
Di-vacancy binding energy	E_B^{2v}	0.22 eV	[39]
Di-interstitial binding energy	E_B^{2i}	1.42 eV	[39]
Pre-exponential interstitial diffusion coefficient			
Along the *c*-axis	$D_{0i\langle c\rangle}$	4.7×10^{-8} m^2 s^{-1}	[39]
Along the *a*-axis	$D_{0i\langle a\rangle}$	3.5×10^{-8} m^2 s^{-1}	[39]
Recombination radius	r_{iv}	10^{-9} m	[39]
Interstitial/dislocation elastic interaction	Z_d^i	1.1	[39]
Vacancy/dislocation elastic interaction	Z_d^v	1.0	[39]
Dislocation line density	ρ	10^{12} m^{-2}	[39]
Burgers vector (prismatic loops)	b	3.23×10^{-10} m	[39]
Atomic volume	V_{at}	2.33×10^{-29} m^3	[39]

The evolution of the fraction of vacancy and interstitial loops during the heat treatment has also been computed and is compared to experimental values in Table 4. The modelling is in rather good agreement with experimental results. Indeed the model is able to reproduce the progressive disappearing of the interstitial loops and the fact that only large vacancy loops remain after the heat treatment performed at 400 and 450 °C.

From the irradiation hardening equation (Eq. (2)), it is also possible to compute the microhardness evolution during the heat treatment using the coefficient $CM\alpha\mu b = 5.4 \times 10^{-9}$ kg mm^{-1}, the hardness evolution at 400 °C and 450 °C is presented in Fig. 1. It can be seen that the predicted hardness is too high for recovery performed at 350 °C compared to the experiment and is slightly too low for recovery performed at 450 °C.

4.3. Validation of the model on experimental results obtained by Adamson and Bell [17]

In order to benchmark the modelling, the heat treatments performed by Adamson and Bell [17] on neutron irradiated recrystallized Zircaloy-2 samples have been computed. One hour heat treatments have been performed at temperatures of 100, 200, 300, 400, 500 and 600 °C. The same heat treatments have been computed using the cluster dynamic model. It can be seen on Figs. 7 and 8 that the modelling is in correct agreement with the experimental results obtained by Adamson and Bell [17] although the initial loop density differs from Adamson results. This shows that although the model has been fitted only in the temperature range of 350–450 °C for long term heat treatments, it is able to predict correctly the microstructure evolution for 1 h heat treatments in a wide temperature range (100–600 °C).

4.4. Analysis of the numerical results and comparison with the loop recovery theory

In order to have a better understanding of the microstructure evolution during the heat treatment, the detailed results of the numerical simulations have been studied. The evolution of the distributions of vacancy and interstitial loops during the heat treatment at 400 °C is shown on Fig. 9. The loop size distribution function ($f(d) = \pi d b C_{n\theta}/V_{at}$ in m^{-3} nm^{-1}, where d is the loop diameter), that can be computed from the values of the size distribution function of clusters of size n ($C_{n\theta}$), is represented on Fig. 9. It can be seen on Fig. 9 that the vacancy loops grow but their density decreases during the annealing while the interstitial loops shrink and progressively disappear.

This difference in the evolution of interstitial and vacancy loops can be studied in details using the numerical model by analyzing only one class of interstitial and vacancy loops. Let us first consider a class of loops, for instance all the vacancy loops with d = 34 nm diameter and all the interstitial loops with d = 16 nm diameter. By using the cluster dynamic model it is possible to compute, at each time step, the net flux of point defects on these classes of loops. The net fluxes of point defects coming towards, respectively all the vacancy loops and the interstitial loops with size n are expressed as:

$$J_{nv} = \left(-\alpha_{nv}^v + \beta_{nv}^v C_{1v} - \beta_{nv}^i C_{1i}\right) C_{nv}$$
$$J_{ni} = \left(-\alpha_{ni}^i - \beta_{ni}^v C_{1v} + \beta_{ni}^i C_{1i} + \alpha_{ni}^v\right) C_{ni} \quad (14)$$

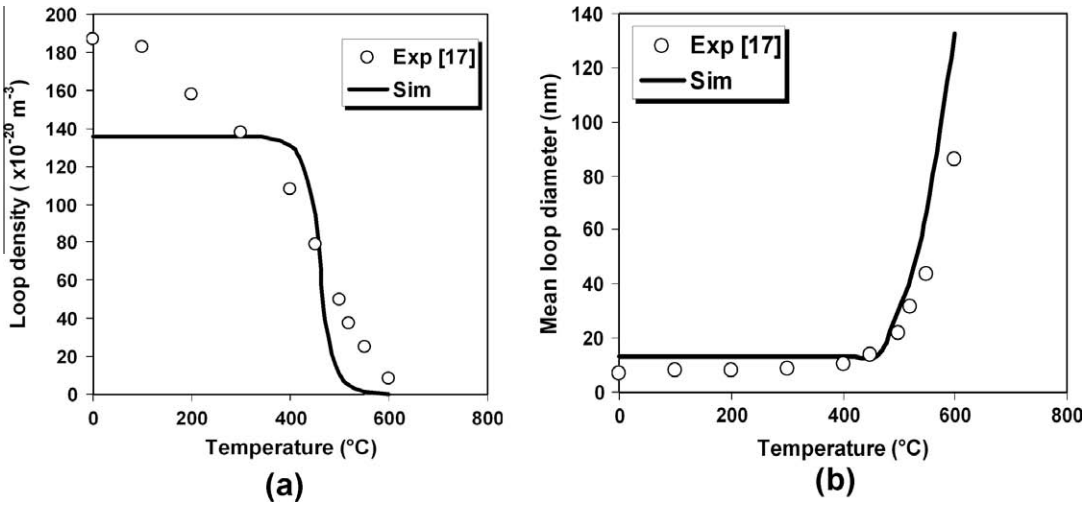

Fig. 7. Comparison between the results of Adamson and the results of the dynamic clusters model: (a) loop density and (b) loop diameter.

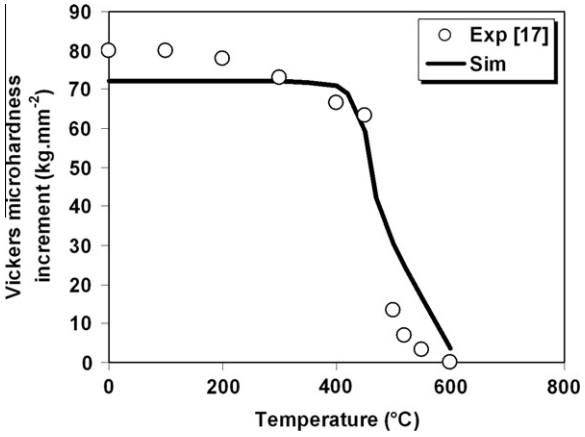

Fig. 8. Comparison between the results of Adamson and Bell [17] and the results of the dynamic clusters model: microhardness increment.

These net fluxes J_{nv} and J_{ni} are shown on Fig. 10. It can be seen on Fig. 10b that the net flux of vacancies coming out of the interstitial loops is always negative. This means that the absorption of vacancies and the emission of SIA are greater than the absorption of SIA and the emission of vacancies. As a consequence interstitial loops with d = 16 nm diameter always tend to shrink. A detailed look at the emission and absorption rate shows that SIA emission and absorption always remain negligible.

Concerning the vacancy loops, it can be seen on Fig. 10a that the net flux of vacancies coming towards vacancy loops with diameter d = 34 nm is first positive then becomes negative (after 500 h), showing that the vacancy loops with d = 34 nm diameter first tend to grow then tend to shrink. This phenomenon can be understood in terms of critical diameter as discussed previously. Indeed, at the beginning of the heat treatment because of the thermal emission of vacancies by loops, the vacancies are in high super-saturation giving a small critical diameter according to Eq. (8). The vacancy loops with diameter higher than this critical diameter grow and the vacancy loops smaller than this critical diameter shrink. As the annealing proceeds the vacancy super-saturation decreases, as shown on Fig 10a, and thus the critical diameter increases leading to the growth of larger loops and to the shrinkage of smaller loops. This induces a progressive drift in the vacancy loop distribution toward larger diameter as illustrated in Fig. 9a.

In order to check the consistency of the numerical modelling with the theory of loop recovery, the evolution of the critical diameter has been estimated at each time step all along the computation of the heat treatment. The critical diameter corresponds, in the computation, to the size of the vacancy loops that have a zero net flux of vacancies (J_{nv} = 0). At the same time step, the vacancy super-saturation (c_v/c_v^0) is also evaluated thanks to the modelling. The evolution of the critical diameter as a function of the vacancy

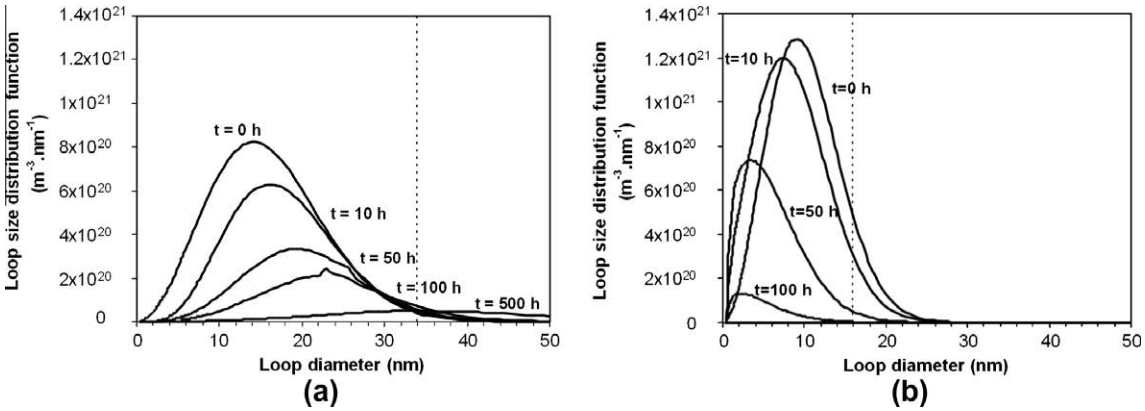

Fig. 9. Evolution of: (a) vacancy and (b) interstitial loop size distribution function during a heat treatment at 400 °C.

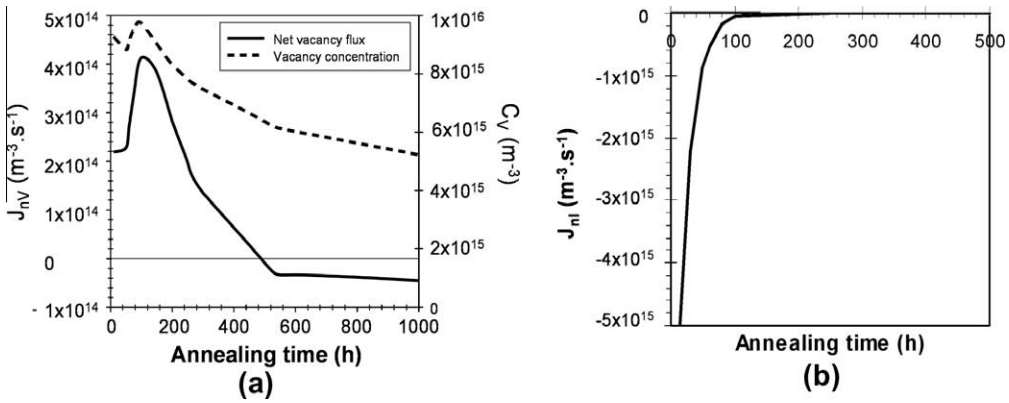

Fig. 10. Evolution of the net flux point defects for: (a) vacancy loops with diameter d = 34 nm and (b) interstitial loops with diameter d = 16 nm during a heat treatment at 400 °C. The evolution of the vacancy concentration is also shown in (a).

super-saturation can then be compared to the theory of the loop recovery (Eq. (9)). However, as it is explained in [28], in the modelling used in this study the binding energy of a vacancy with a vacancy loop is given by an empirical formula (Eq. (15)) obtained from Molecular Dynamic computations [49] instead of the elastic binding energy that is not rigorous for very small clusters.

$$E_{nv}^{Bv} = E_v^f + \frac{E_{2v}^B - E_v^f}{2^{2/3}-1}\left[n^{2/3} - (n-1)^{2/3}\right] \tag{15}$$

It has been checked that, in the case of zirconium alloys, for large n, the Eq. (15) is in good agreement with the expression given by the elastic theory of dislocations (Eq. (16)) obtained from the elastic energy of a circular loop (Eq. (16)) [23] using the values ν = 0.35, μ = 28 GPa at 400 °C given in the literature for zirconium alloys [36].

$$E_{elas}^B = E_f - \frac{\mu b V_{at}}{4\pi(1-\nu)r}\ln\left(\frac{4r}{b}\right) \tag{16}$$

In order to compute the super-saturation (c_v/c_v^0) of vacancies as a function of the critical diameter from the recovery theory [35], it is necessary to introduce the exact formula used in the modelling for the energy release per vacancy emitted by a vacancy loop. The energy release per vacancy emitted by a vacancy loop used is therefore:

$$w = E_{nv}^{Bv} - E_v^f = \frac{E_{2v}^B - E_v^f}{2^{2/3}-1}\left[n^{2/3} - (n-1)^{2/3}\right] \tag{17}$$

Thus the super-saturation of vacancies can be expressed as:

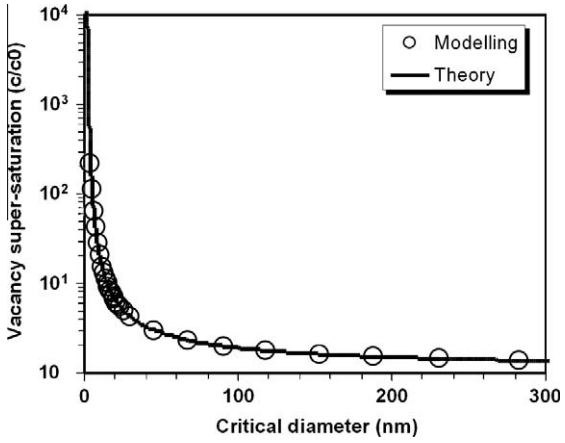

Fig. 11. Comparison of the vacancy super-saturation obtained as a function of the critical diameter using the modelling and the theory for loop recovery.

$$\ln\left(\frac{c}{c_0}\right) = \frac{w}{kT} = \frac{1}{kT}\frac{E_{2v}^B - E_v^f}{2^{2/3}-1}\left[n^{2/3} - (n-1)^{2/3}\right] \tag{18}$$

with $n = \pi r_{crit}^2 b/V_{at}$.

The values of the computed vacancy super-saturation as a function of the computed critical diameter are compared to the Eq. (18) given by the recovery theory (Fig. 11). It is seen on Fig. 11 that the cluster dynamic modelling described here is consistent with the theory for loop recovery.

5. Conclusion

This study was devoted to the recovery of the irradiation damage in recrystallized zirconium alloys. A thorough experimental study of the irradiation damage recovery has been performed using both hardness tests and TEM observations after various heat treatments. The TEM observations have shown that the loops created by irradiation are annealed during the heat treatment. More precisely it is observed that the loop density decreases while the loop size increases. A detailed TEM study, using the inside/outside contrast method, has been able to show that the interstitial loop recovery is faster than the vacancy loop recovery. At the end of a long heat treatment at high temperature only large vacancy loops in very low density remain in the material. This phenomenon is consistent with the loop recovery theory based on vacancy bulk diffusion where all the interstitial loops progressively shrink and the smallest vacancy loops also shrink at the expense of the largest vacancy loops.

A cluster dynamic model has been used to reproduce and predict the evolution of the loop microstructure during the heat treatment. A fair agreement has been obtained between the experimental results and the simulation. This model is also in good agreement with experimental results given in the literature and is consistent with the theory for loop recovery.

This numerical model gives a valuable tool to predict the evolution of the microstructure during long term heat treatment such as the dry cask transportation or dry storage of the spent fuel assembly.

This experimental and numerical study is a first step toward the understanding and the prediction of the post-irradiation creep behaviour of recrystallized zirconium alloys when a coupling between the deformation and the annealing of the radiation damage occurs.

Acknowledgement

The authors are greatly indebted to AREVA NP for providing the materials.

Appendix A. Equations of the cluster dynamic model

The cluster dynamic model used in this study is the anisotropic cluster dynamic model presented in details in [29]. However, for our purpose, since the radiation damage recovery implies essentially the bulk diffusion of vacancies which is isotropic, only the model based on isotropic diffusion of point defects [28] is described here. The evolution of the cluster distribution is given by the integration of the discrete rate equations Eqs. (A.1.a), (A.1.b) and (A.1.c). However, in order to be able to compute the evolution of large clusters up to long irradiation or recovery time, it is necessary to change these discrete equations into the continuous Fokker–Plank type equations given in Eqs. (A.2.a), (A.2.b), and (A.2.c).

In the modelling it is assumed that only self-interstitial atoms (SIA) and vacancies are mobile [28]. It is also assumed that the only point defect clusters present in the material are both vacancy and interstitial loops. In the equations, only the emission of vacancies by vacancy loops is taken into account, the emission of SIA by vacancy loops is neglected due to the high formation energy of the interstitial. On the other hand, interstitial loops can emit both SIA and vacancies. Nevertheless, as it is described in [28], it was assumed that only large interstitial loops ($n > 40$) can emit vacancies. Therefore this contribution is not taken into account in the discrete equations used for small loops but only taken into account in the continuous Fokker–Plank equations.

A.1. Rate equations

A.1.1. Discrete equations

$$\left.\begin{aligned}\frac{dC_{ni}}{dt} &= G_{ni} + \left[\beta^i_{(n-1)i}C_{1i}\right]C_{(n-1)i} + \left[\beta^v_{(n+1)i}C_{1v} + \alpha^i_{(n+1)i}\right]C_{(n+1)i} - \left[\alpha^i_{ni} + \beta^v_{ni}C_{1v} + \beta^i_{ni}C_{1i}\right]C_{ni}\\ \frac{dC_{nv}}{dt} &= G_{nv} + \left[\beta^v_{(n-1)v}C_{1v}\right]C_{(n-1)v} + \left[\beta^i_{(n+1)v}C_{1i} + \alpha^v_{(n+1)v}\right]C_{(n+1)v} - \left[\alpha^v_{nv} + \beta^v_{nv}C_{1v} + \beta^i_{nv}C_{1i}\right]C_{nv}\end{aligned}\right\}, \quad 40 > n > 2 \tag{A.1.a}$$

$$\left.\begin{aligned}\frac{dC_{1i}}{dt} &= G - R_{iv}C_{1i}C_{1v} - K^i_dC_{1i} - K^i_sC_{1i} - 4\beta^i_{1i}C_{1i}C_{1i} + 4\alpha^i_{2i}C_{2i} + \beta^v_{2i}C_{1v}C_{2i} - C_{1i}\sum_{n=2}\beta^i_{ni}C_{ni} - C_{1i}\sum_{n=2}\beta^i_{nv}C_{nv} + \sum_{n=3}\alpha^i_{ni}C_{ni}\\ \frac{dC_{1v}}{dt} &= G - R_{iv}C_{1i}C_{1v} - K^v_dC_{1v} - K^v_sC_{1v} - 4\beta^v_{1v}C_{1v}C_{1v} + 4\alpha^v_{2v}C_{2v} + \beta^i_{2v}C_{1i}C_{2v} - C_{1v}\sum_{n=2}\beta^v_{nv}C_{nv} - C_{1v}\sum_{n=2}\beta^v_{ni}C_{ni} + \sum_{n=3}\alpha^v_{nv}C_{nv}\end{aligned}\right\}, \quad n = 1 \tag{A.1.b}$$

$$\left.\begin{aligned}\frac{dC_{2i}}{dt} &= 2\beta^i_{1i}C_{1i}C_{1i} - 2\alpha^i_{2i}C_{2i} - \beta^i_{2i}C_{1i}C_{2i} + \alpha^i_{3i}C_{3i} - \beta^v_{2i}C_{1v}C_{2i} + \beta^v_{3i}C_{1v}C_{3i}\\ \frac{dC_{2v}}{dt} &= 2\beta^v_{1v}C_{1v}C_{1v} - 2\alpha^v_{2v}C_{2v} - \beta^v_{2v}C_{1v}C_{2v} + \alpha^v_{3v}C_{3v} - \beta^i_{2v}C_{1i}C_{2v} + \beta^i_{3v}C_{1i}C_{3v}\end{aligned}\right\}, \quad n = 2 \tag{A.1.c}$$

with

n	is the number of point defects in a loop with size n. The radius of the loop with size n is given by $r_n = \sqrt{nV_{at}/\pi b}$. V_{at} is the atomic volume and b is the Burgers vector of the loop. In our case only $\langle a\rangle$ type loops are considered
$C_{n\theta}$	the concentration of loops with size n; $\theta = i$ for interstitial loop and $\theta = v$ for vacancy loop
$\beta^{\theta'}_{n\theta}C_{1\theta'}$	absorption frequency of point defects of type θ' by loop of type θ
$\alpha^{\theta'}_{n\theta}$	emission frequency of point defects of type θ' by a loop of type θ
G	the production rate of point defects (Frenkel pairs) ($m^{-3}\ s^{-1}$). It takes into account the creation of point defects inside displacements cascade under irradiation
$G_{n\theta}$	the production rate of point defects clusters. It takes into account the creation of point defects clusters inside displacements cascade under irradiation
R_{iv}	the recombination rate of point defects
$K^\theta_dC_{1\theta}$	the elimination rate of point defects θ on dislocations lines present before irradiation
$K^\theta_sC_{1\theta}$	is the elimination rate of point defects θ on surfaces or grain boundaries

A.1.2. Continuous equations

For cluster size larger than $n \geqslant N_C$, with $N_C = 40$ in our case, the Fokker–Planck type equations (Eq. (A.2.a)) are used.

$$\frac{\partial C_\theta(x)}{dt} = \frac{\partial}{\partial x}\left[f_\theta(x)C_\theta(x)\right] + \frac{\partial^2}{\partial x^2}\left[d_\theta(x)C_\theta(x)\right] \tag{A.2.a}$$

where $C_\theta(x)$ is the size distribution function of the cluster with size x, x being the number of monomers in the cluster. The size of the cluster, x, is now a continuous variable which is expressed as:

$$\begin{aligned}u &= (m - N_C)\ln(C)\\ x &= N_C + \frac{1}{C-1}\left[\exp(u) - 1\right]\end{aligned} \tag{A.2.b}$$

where m is the equation number, or class number, of the continuous equations ($40 \leqslant m \leqslant 300$ for vacancy and interstitial loops), N_C is the maximum number of monomers for discrete equations ($N_C = 40$) and C is a constant greater than unity that can be chosen conveniently and is equal to $C = 1.06$ in our case. The Fokker–Planck equations are thus discretised in the x space in such way that the increment of Δx between two successive points in the x space increases when x increases. This method has the great advantage to allow the computation for long term evolution of very large clusters. The functions $f_\theta(x)$ and $d_\theta(x)$ correspond to the transition rates and are given by Eqs. (A.2.c) and (A.2.d), respectively for vacancy and interstitial clusters.

$$\begin{aligned}d_v(x) &= \frac{1}{2}\left[\beta^v_{xv}C_{1v} + \beta^i_{xv}C_{1i} + \alpha^v_{xv}\right],\\ f_v(x) &= \beta^v_{xv}C_{1v} - \beta^i_{xv}C_{1i} - \alpha^v_{xv}\end{aligned} \tag{A.2.c}$$

$$\begin{aligned}d_i(x) &= \frac{1}{2}\left[\beta^i_{xi}C_{1i} + \beta^v_{xi}C_{1i} + \alpha^i_{xi} + \alpha^v_{xi}\right],\\ f_i(x) &= \beta^i_{xi}C_{1i} - \beta^v_{xi}C_{1v} - \alpha^i_{xi} + \alpha^v_{xi}\end{aligned} \tag{A.2.d}$$

In the continuous equations the term α^v_{xi} describing the thermal emission of vacancies from interstitial clusters has been added because for large clusters this term is no more negligible at high temperature.

A.2. Recombination rate

The recombination rate of point defects is given by Eq. (A.3).

$$R_{iv} = 4\pi r_{iv}(D_i + D_v) \tag{A.3}$$

where $D_\theta = D_{\theta 0}\exp(-E^m_\theta/kT)$ is the diffusion coefficient of the point defect of type θ with $D_{\theta 0}$ the frequency factor, E^m_θ the migration energy and r_{iv} the recombination radius.

A.3. Rate coefficient for dislocations

The elimination rate of point defects on dislocations is given by Eq. (A.4)

$$K^\theta_d C_{1\theta} = \rho Z^\theta_d D_\theta C_{1\theta} \tag{A.4}$$

where ρ is the dislocation density and Z^θ_d the capture efficiency of point defect of type θ by dislocations. Z^θ_d is taken equal to 1 for vacancies and 1.1 for SIA.

A.4. Rate coefficients for absorption of point defects by loops

The absorption frequency of point defects of type θ' by loop of type θ is given by Eq. (A.5)

$$\beta^{\theta'}_{n\theta} C_{1\theta'} = 2\pi r_n Z^{\theta'}_{n\theta} D_{\theta'} C_{1\theta'} \tag{A.5}$$

In Eq. (A.5) $Z^{\theta'}_{n\theta}$ is an efficiency factor that allows taking the defect-dislocation elastic interaction and also the toroidal shape of the loop into account; $Z^{\theta'}_{n\theta}$ depends on the loop size according to Eq. (A.6) [29].

$$Z^{\theta'}_{n\theta} = Z^{\theta'}_d Max\left(\frac{2\pi}{\ln(8r_n/r_p)}; 1\right) \tag{A.6}$$

where r_p is the pipe radius, taken as $r_p = 2b$.

A.5. Rate coefficient for emission of point defects by loops

The rate of emission of a point defect of type θ' by a cluster of type $n\theta$ ($\alpha^{\theta'}_{n\theta}$) is given by Eq. (A.7).

$$\alpha^{\theta'}_{n\theta} = 2\pi \frac{r_{n-1}}{V_{at}} Z^\theta_{(n-1)\theta} D_\theta \exp\left(-E^{B\theta'}_{n\theta}/kT\right) \tag{A.7}$$

where $E^{B\theta'}_{n\theta}$ is the binding energy of the point defect θ' with the cluster $n\theta$. The binding energy is computed from the empirical formula (Eq. (A.8)) obtained from Molecular Dynamic computations [34].

$$E^{B\theta}_{n\theta} = E^f_\theta + \frac{E^B_{2\theta} - E^f_\theta}{2^{2/3} - 1}\left[n^{2/3} - (n-1)^{2/3}\right] \quad \text{for } \theta' = \theta \tag{A.8.a}$$

$$E^{B\theta'}_{n\theta} = E^f_{\theta'} - \frac{E^B_{2\theta} - E^f_\theta}{2^{2/3} - 1}[n^{2/3} - (n-1)^{2/3}] \quad \text{for } \theta' \neq \theta \tag{A.8.b}$$

where E^f_θ and $E^B_{2\theta}$ are the formation energy of the point defect θ and the binding energy between two point defects θ.

A.6. Rate coefficients for grain boundaries

In order to compute the absorption rate by the grain boundaries the multiple sink effect as to be taken into account [28]. The sink strength of the whole medium for θ point defects (S^θ_m) can be computed as:

$$S^\theta_m = \rho Z^\theta_d + \frac{1}{D_\theta}\sum_{n=2}(\beta^\theta_{n\theta} + \beta^\theta_{n\theta'})C_{n\theta} \tag{A.9}$$

Then the absorption rate by the grain boundaries can be expressed as:

$$K^\theta_s C_{1\theta} = 6\frac{\sqrt{S^\theta_m}}{d_g} D_\theta C_{1\theta} \tag{A.10}$$

where d_g is the diameter of the grain taken from experimental observations as $d_g = 10\ \mu m$.

Appendix B. Introduction of the initial microstructure

In the modelling it has been chosen to introduce an "ad hoc" initial microstructure in the form of analytical loop size distribution functions corresponding to the microstructure observed by TEM after irradiation. However, since the experimental distribution of the loop size distribution is incomplete (only the loops with diameter higher than 2 nm are observed and no determination of the size distribution of vacancy and interstitial loops separately is performed) assumptions have to be made concerning the details of the loop size distribution functions. First, it is chosen to use a simple Maxwell–Boltzmann distribution function for the loop size distribution of both vacancy and interstitial loops (Fig. B.1a). It can be seen on Fig. B.1b that the cumulated distribution function of the Maxwell–Boltzmann distribution is in good agreement with the experimental TEM observations. It has to be noticed that other types of equivalent distribution functions have also been tested and give similar results. The Maxwell–Boltzmann size distribution function chosen ($f_\theta(r)$ where r is the loop radius) for loops of type θ and with density N_θ (in m^{-3}) is given by:

$$f_\theta(r) = N_\theta \frac{1}{\sigma^3_\theta}\sqrt{\frac{2}{\pi}} r^2 \exp\left(-\frac{r^2}{2\sigma^2_\theta}\right) \tag{B.1}$$

$$\text{with } \int_0^\infty f_\theta(r)dr = N_\theta \quad \text{and} \quad \langle r_\theta\rangle = \frac{1}{N_\theta}\int_0^\infty f_\theta(r) r\, dr = 2\sigma_\theta\sqrt{\frac{2}{\pi}}$$

The initial microstructure is introduced as an input file in the form of the concentration of loops with size n ($C_{n\theta}$) as a function of n calculated according to the following formula:

$$C_{n\theta} = \frac{V_{at}}{b}\frac{1}{2\pi r_n} f_\theta(r_n) \tag{B.2}$$

$$\text{with} \quad r_n = \sqrt{nV_{at}/\pi b}$$

It is first assumed that the initial microstructure is composed of 50% vacancy loops and 50% interstitial loops leading therefore to: $N_i = N_v$.

The total loop density measured in this work is $1.2 \times 10^{22}\ m^{-3}$. However Adamson and Bell [17] have measured a higher total loop density of $1.8 \times 10^{22}\ m^{-3}$ on recrystallized Zircaloy-2. This difference could be due to the effect of niobium on loop nucleation [47,48]. An intermediate value of $1.4 \times 10^{22}\ m^{-3}$ is chosen here leading to $N_i = N_v = 7 \times 10^{21}\ m^{-3}$.

The initial loop size distribution has been estimated by TEM, despite the difficulty of the observations with such a high loop density. The cumulated initial loop size distribution is given in Fig. B.1b. A mean diameter of 14 nm has been obtained in this work but Adamson and Bell [17] have estimated a lower value close to 10 nm. An intermediate value of 13 nm is chosen here. However, it is not known whether the vacancy loops have a mean diameter higher than the interstitial loops for the initial state. Values of $\sigma_v = 5.0$ nm and $\sigma_i = 3.2$ nm are chosen here leading to a mean diameter of 16.0 nm for vacancy loops and a mean diameter of 10.2 nm for interstitial loops. It can be seen on Fig. B.1b that the analytical total loop distribution, computed by adding the vacancy and the interstitial loop distributions, is in good agreement with the experimental loop distribution. It has to be pointed out that the results of the computation of the heat treatment depends only slightly on the choice of the initial distribution, for a given mean

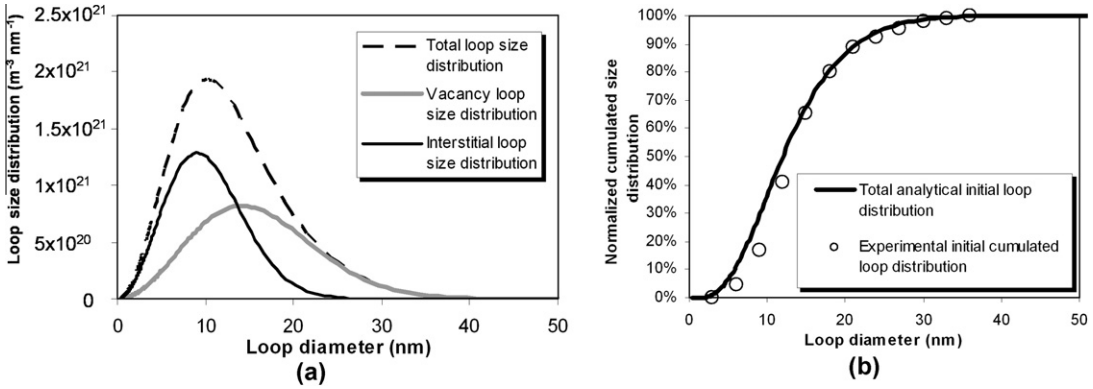

Fig. B.1. (a) Analytical loop size distributions for both vacancy and interstitial loops. The total loop size distribution is also shown on the figure. (b) Total analytical initial loop distribution compared to the experimental as-irradiated cumulated loop distribution.

diameter and loop density, provided that the mean diameter of vacancy loops remains higher than the mean diameter of interstitial loops.

References

[1] C. Cappelaere, R. Limon, D. Gilbon, T. Bredel, O. Rabouille, P. Bouffioux, J.P. Mardon, in: G.D. Moan, P. Rudling (Eds.), Zirconium in the Nuclear Industry: 13th International Symposium, ASTM STP 1423, ASTM International, West Conshohocken, PA, 2002, p. 720.
[2] J. Ribis, F. Onimus, J.-L. Béchade, S. Doriot, C. Cappelaere, C. Lemaignan, A. Barbu, O. Rabouille, J. ASTM Int. 5 (3) (2009).
[3] D.O. Northwood, R.W. Gilbert, L.E. Bahen, P.M. Kelly, R.G. Blake, A. Jostsons, P.K. Madden, D. Faulkner, W. Bell, R.B. Adamson, J. Nucl. Mater. 79 (1979) 379.
[4] M. Griffiths, J. Nucl. Mater. 159 (1988) 190.
[5] C. Lemaignan, A.T. Motta, Zirconium alloys in nuclear applications, nuclear materials, in: B.R.T. Frost (Ed.), in: R.W. Cahn, P. Haasen, E.J. Kramer (Eds.), Materials Science and Technology Series, vol. 10B, VCH, New York, 1994, pp. 1–51.
[6] H.R. Higgy, F.H. Hammad, J. Nucl. Mater. 44 (1972) 215.
[7] C.J. Baroch, Properties of Reactor Structural Alloys after Neutron or Particle Irradiation, in: ASTM STP 570, 1975, p. 129.
[8] T. Yasuda, M. Nakatsuka, K. Yamashita, in: Zirconium in the Nuclear Industry: 7th International Symposium, ASTM STP 939, 1987, p. 734.
[9] A.J.E. Foreman, Philos. Mag. 17 (1968) 353.
[10] P.B. Hirsch, in: Proceedings of a Conference on "Point Defect Behaviour and Diffusional Processes" Organized by the Metals Society and Held at the Royal Fort, University of Bristol, on 13–16 September, 1976, The Metals Society, London, 1977, p. 95.
[11] F. Onimus, I. Monnet, J.L. Béchade, C. Prioul, P. Pilvin, J. Nucl. Mater. 238 (2004) 165.
[12] L.M. Howe, W.R. Thomas, J. Nucl. Mater. 2 (3) (1960) 248.
[13] C.C. Dollins, Radiat. Effects 6 (1972) 271.
[14] K. Snowden, K. Veevers, Radiat. Effects 20 (1973) 169.
[15] T. Torimaru, T. Yasuda, M. Nakatsuka, J. Nucl. Mater. 238 (1996) 169.
[16] G.J.C. Carpenter, J.F. Watters, in: Zirconium in the Nuclear Industry: ASTM STP 551, 1974, p. 400.
[17] R.B. Adamson, W.L. Bell, Microstructure and mechanical behaviour of materials, in: International Symposium, Xian, China, vol. 1, 1985, p. 237.
[18] P.M. Kelly, R.G. Blake, Philos. Mag. 28 (1973) 415.
[19] E. Tenckhoff, in: ASTM STP 966, ASTM International, West Conshohocken, PA, 1988.
[20] M. Nakatsuka, M. Nagai, J. Nucl. Sci. Technol. 24 (1987) 832.
[21] B. Edmondson, G.K. Williamson, Philos. Mag. 9 (1964) 277.
[22] D.M. Maher, B.L. Eyre, Philos. Mag. 23 (1967) 409.
[23] A. Jostsons, P.M. Kelly, R.G. Blake, J. Nucl. Mater. 66 (1977) 236.
[24] M.J. Makin, F.J. Minter, S.A. Manthorpe, Philos. Mag. 13 (1996) 729.
[25] G.S. Was, Fundamentals of Radiation Materials Science (Metals and Alloys), Springer Verlag, 2007.
[26] J.T. Busby, M.C. Hash, G.S. Was, J. Nucl. Mater. 336 (2005) 267.
[27] D.O. Northwood, I.M. London, L.E. Bahen, J. Nucl. Mater. 55 (1975) 299.
[28] J.H. Moon, P.E. Cantonwine, K.R. Anderson, S. Karthikeyan, M.J. Mills, J. Nucl. Mater. 353 (2006) 177.
[29] J.L. Derep, S. Ibrahim, R. Rouby, G. Fantozzi, Acta Metall. 28 (1979) 607.
[30] S. Doriot, D. Gilbon, J.-L. Béchade, M.-H. Mathon, L. Legras, J.-P. Mardon, J. ASTM Int. 2 (2005) 175.
[31] G. Monnet, Acta Mater. 55 (2007) 5081.
[32] J. Friedel, Dislocations, in: R. Smolucowski, N. Kurti (Eds.), Pergamon Press, 1964.
[33] J.A. Turnbull, M.S. Stagg, Philos. Mag. 14 (1966) 1049.
[34] F. Kroupa, J. Silcox, M.J. Whelan, Philos. Mag. 6 (1971) 971.
[35] B.L. Eyre, D.M. Maher, Philos. Mag. 24 (1971) 767.
[36] J.P. Hirth, J. Lothe, Theory of Dislocations, John Wiley and sons, New York, 1982.
[37] B. Burton, M.V. Speight, Philos. Mag. A 53 (1986) 385.
[38] A. Hardouin Duparc, C. Moingeon, N. Smetniansky-de-Grande, A. Barbu, J. Nucl. Mater. 302 (2002) 143.
[39] F. Christien, A. Barbu, J. Nucl. Mater. 346 (2005) 272.
[40] F. Christien, A. Barbu, J. Nucl. Mater. 393 (2009) 153–161.
[41] V. Dubinko, A. Turkin, A. Abyzov, M. Griffiths, J. ASTM Int. 2 (2005) 157.
[42] D.L. Douglass, Atomic Energy Review, Supplement 1971, IAEA, Vienna, 1971, p. 277.
[43] G.M. Hood, R.J. Schultz, Acta Met. 22 (1974) 459.
[44] J. Horvath, F. Dyment, H. Mehrer, J. Nucl. Mater 126 (1984) 206.
[45] G.M. Hood, J. Nucl. Mater. 159 (1988) 149.
[46] R.A. Perez, M. Weissmann, J. Nucl. Mater. 374 (2008) 95.
[47] D.O. Northwood, Atom. Energy Rev. 15 (1977).
[48] C. Hellio, C.H. de Novion, L. Boulanger, J. Nucl. Mater. 159 (1988) 368.
[49] N. Soneda, T. Diaz de la Rubia, Philos. Mag. A 78 (1998) 995.